P wave anisotropy caused by partial eclogitization of descending crust demonstrated by modelling effective petrophysical properties

Sascha Zertani[1]*, Johannes C. Vrijmoed[1], Frederik Tilmann[1,2], Timm John[1]*, Torgeir B. Andersen[3], & Loic Labrousse[4]

[1]Institute of Geological Sciences, Freie Universität Berlin, 12249, Berlin, Germany.

[2]Deutsches GeoForschungsZentrum, 14473, Potsdam, Germany.

[3]The Centre of Earth Evolution and Dynamics (CEED), Department of Geosciences, University of Oslo, 0316 Oslo, Norway.

[4]Sorbonne Université, CNRS-INSU, Institut des Sciences de la Terre Paris, ISTeP, UMR 7193, F-75005 Paris, France.

Corresponding authors:

Sascha Zertani, Department of Geosciences, Freie Universität Berlin, Malteserstr. 74-100, 12249, Berlin, Germany. E-mail address: sascha.zertani@fu-berlin.de. Telephone: +49 30 838 75782.

and

Timm John, Department of Geosciences, Freie Universität Berlin, Malteserstr. 74-100, 12249, Berlin, Germany. E-mail address: timm.john@fu-berlin.de. Telephone: +49 30 838 70103.

Key Points:

- Eclogitization of crustal rocks causes significant anisotropy on a crustal scale
- Geometric arrangement has no significant influence on effective seismic properties
- Backazimuthal bias in receiver function studies can be caused by eclogitization

Abstract

Seismological studies of large-scale processes at active convergent plate boundaries typically probe lower crustal structures with wavelengths of several kilometers, whereas field-based studies typically sample the resulting structures at a much smaller scale. To bridge this gap between scales we derive effective petrophysical properties on the 20-m, 100-m, and kilometer scales based on numerical modelling with the Finite Element Method. Geometries representative of eclogitization of crustal material are extracted from the partially eclogitized exposures on the island of Holsnøy (Norway). We find that the P wave velocity is controlled by the properties of the constituent lithologies rather than their geometric arrangement. P wave anisotropy, however, is dependent on the fabric orientation of the associated rocks, as fabric variations cause changes in the orientation of the initial anisotropy. As a result, different structural associations can result in effective anisotropies ranging from ~0-4% for eclogites not associated with ductile deformation to up to 8% for those formed during ductile deformation. For the kilometer-scale structures, a scale that in principle can be resolved by seismological studies, we obtained P wave velocities between 7.7 and 8.1 km s-1. The effective P wave anisotropy on the kilometer-scale is ~5% and thus explains the backazimuthal dependence of seismological images of, for example, the Indian lower crust currently underthrusting beneath the Himalaya. These results imply that seismic anisotropy could be the key to visualize structures in active subduction and collision zones that are currently invisible to geophysical methods and thus unravel the underlying processes active at depth.

1. Introduction

Convergent plate boundaries are among the most important sites of crustal reorganization and element recycling. There, crustal material is buried to great depths, recycled into the mantle, integrated into orogenic roots and in some cases also exhumed back to the surface. All of these processes result in the modification of crustal rocks through metamorphism and brittle and/or ductile deformation. However, these processes occur at depths inaccessible to direct observation. Thus, the structures that develop at depth are either studied by geophysical imaging methods or by investigating exhumed rocks that have been metamorphosed and/or deformed in the past (e.g., Austrheim, 1987; Rondenay et al., 2008). Field-based studies of deep processes are restricted to rare exposures where mineral assemblages and structures are not substantially overprinted during exhumation (e.g., Austrheim, 1987; John & Schenk, 2003). In order to properly interpret seismic velocities in terms of metamorphic processes associated with large-scale tectonics such as

continental collision and subduction of oceanic plates we require knowledge of how seismic properties change with depth and lithology (e.g., Kind et al., 2012; Rondenay et al., 2008). However, while field-based studies include information down to the micron scale, geophysical imaging techniques employ wavelengths that are only sensitive to kilometer-scale structures (e.g., Bloch et al., 2018; Kim et al., 2019). In addition, the resolution of geophysical imaging is often further limited by the available station coverage and distribution of signal sources. This creates a large gap between the scale at which we image structures with geophysical methods and the scale at which we can observe structures in the field. Subsequently, seismic velocities that are measured in the laboratory or calculated for individual samples may not be representative of the properties of lithological and structural associations on a larger scale. As these structures are smaller than the resolution of seismological methods the properties of the different constituents will act together averaging to one effective medium (e.g., Backus, 1962; Hudson, 1981).

Specifically, eclogitization processes occurring at depth remain difficult to assess, although they are suspected to play a major role in geodynamic processes (Austrheim, 1991; Dewey et al., 1993; Yamato et al., 2019). Eclogitization causes a density increase of crustal material that decreases buoyancy forces and significantly adds to driving forces (e.g., slab pull) at convergent plate boundaries (e.g., Hetényi et al., 2007; Klemd et al., 2011). However, the same density increase also significantly complicates the detection of eclogites at depth as it is combined with an increase of the elastic moduli of the rock. Subsequently, the resulting seismic properties of eclogites become similar to those of mantle peridotites, making a distinction between the mantle and crust at depth difficult (e.g., Bostock, 2013; Hetényi et al., 2007; Rondenay et al., 2008; Yuan et al., 2000). Nevertheless, partially eclogitized material shows a range of geometric

82 configurations and patterns of anisotropy directions in the constituent lithologies, depending on
83 conditions during formation (Raimbourg et al., 2005; Zertani et al., 2019b). It is therefore not
84 necessarily straightforward to simply transform a measured velocity into a degree of
85 eclogitization.
86 Field-based studies have shown that eclogitization of crustal rocks is often associated with fluid
87 availability that enhances mineral reactions and ductile deformation, first forming centimeter-
88 thick shear zones (Austrheim, 1987; John & Schenk, 2003). As eclogitization and deformation
89 progress, such shear zones can widen reaching a thickness of a few hundred meters (Boundy et
90 al., 1997; Raimbourg et al., 2005; Zertani et al., 2019b). In the exposed examples such structures
91 rarely reach scales that can be resolved with geophysical methods and the complex associations
92 would thus act as an effective medium at depth adapting averaged properties of the different
93 lithologies (Zertani et al., 2019a).
94 In contrast, geophysical imaging methods are used to study large-scale processes active at great
95 depth in collision and subduction zones (e.g., Halpaap et al., 2018). To unravel structures caused
96 by metamorphism coeval with deformation, the receiver function method is of specific interest. It
97 is based on the conversion of P to S waves and vice versa at boundaries with contrasting
98 impedance and therefore mostly sensitive to structural boundaries (Kind et al., 2012). For
99 example, Schneider et al. (2013) imaged a low velocity zone below the Pamir corresponding to
100 the subducting lower continental crust of the Eurasian Plate. The velocity contrast of this zone
101 with respect to the surrounding mantle, however, decreases below a depth of ~100 km,
102 suggesting eclogitization of the down going crust. Nabelek et al. (2009) and Schulte-Pelkum et
103 al. (2005) observed a backazimuthal dependence of the retrieved signal in the lower crust of

India beneath the Himalaya that suggests a significant large-scale anisotropic fabric within the lower continental crust of India.

Meanwhile, direct estimates of seismic velocities are usually derived from samples that are only a few centimeters in size (e.g., Kern et al., 1996) and extrapolation to scales that are resolvable using geophysical methods relies on poorly supported assumptions, mainly that the composition of the samples is representative of the crust at geophysically relevant scale and that the large-scale organization of lithologies has no relevance. Voigt-Reuss-Hill averaging is the standard method to calculate velocities within a medium based on the abundance of individual mineral phases resulting in an average (isotropic) seismic velocity (Hill, 1952). The classic Backus averaging allow calculation of the effective anisotropy of a finely layered medium; it is valid under the assumption that the thickness of individual layers is far smaller than the seismic wavelength (Backus, 1962). Although such averaging schemes are widely used to constrain seismic velocities of various rocks, their capabilities are limited because they are only valid for simple geometries that generally do not capture the structural complexity of real rocks.

To assess these simplifying assumptions, it is necessary to utilize a more sophisticated approach. Accordingly, we calculate effective P wave velocities of eclogite-facies associations using a technique based on finite element method (FEM) calculations, for a variety of representative geometries. The simplified geometries are derived from the field observations on the island of Holsnøy in the Bergen Arcs (Norway), where a >70 km² large complex of partially eclogitized lower continental crust is exposed that provides an excellent coherent laboratory to study the geometries that are established during eclogitization.

2. Geological Setting

The exposed lower continental crust on the island of Holsnøy (Bergen Arcs, western Norway)

has been partially eclogitized during the Caledonian orogeny (Austrheim, 1991). The rocks belong to the Lindås nappe, which together with the Dalsfjord and Jotun nappe complexes represents the lower crust of the former Jotun microcontinent, that constituted part of the pre-Caledonian hyperextended margin of Baltica (Andersen et al., 2012; Jakob et al., 2019). The Lindås nappe is for a large part composed of anorthositic granulites that experienced Proterozoic granulite-facies P-T conditions of ~1 GPa and ~800 °C, at ~950 Ma (Austrheim & Griffin, 1985). The P-T conditions in the following ~500 M.y. are unclear. The rocks, however, show no signs of significant alteration before the Scandian Caledonian collision and likely cooled to conditions reflecting mid to lower crustal conditions (Jamtveit et al., 1990).

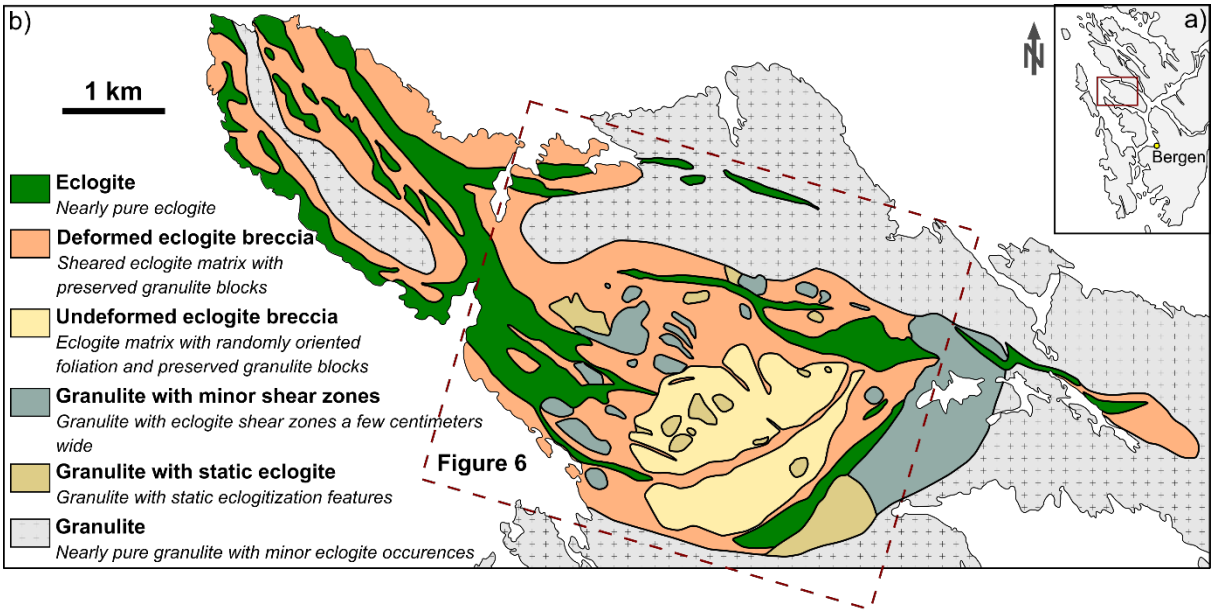

Fig. 1. Geological map of northwestern Holsnøy (modified from Jolivet et al. (2005) and Zertani et al. (2019b)). The inset (a) shows the location of Holsnøy in western Norway.

During the Caledonian collision the Jotun microcontinent constituted the leading edge of Baltica, which was integrated into the collision wedge as the lower plate (Corfu et al., 2014). Subsequently, the Lindås nappe was subjected to peak eclogite-facies conditions of ~2 GPa and ~750 °C at 429 Ma (Bhowany et al., 2018; Glodny et al., 2008; Jamtveit et al., 1990; Zhong et

al., 2019). Large volumes of the dry granulite-facies rocks, however, remained metastable and were thus preserved (Austrheim, 1987; Jackson et al., 2004). Eclogitization is linked to fluid availability and was facilitated along shear zones but also progressed into the rock volume as a static overprint (Austrheim, 1987; Zertani et al., 2019b). Fluid infiltration was likely initiated via brittle fractures, which provided fluid pathways within an otherwise dry rock (Austrheim, 1990; Jamtveit et al., 1990).

This heterogeneously distributed transformation resulted in a complex mixture of eclogites and granulites (Fig. 1). The resulting lithologies can be divided into six categories based on the abundance of eclogite and the associated structural relationships (Boundy et al., 1992; Zertani et al., 2019b). Next to the mostly unaltered granulite (<20 % eclogite), small-scale eclogitization features are distinguished into granulites cut by eclogite-facies shear zones a few centimeters wide and granulites with eclogitized patches that are not associated with ductile deformation (both 20-50 % eclogite). With progressive eclogitization these evolve into the so-called eclogite breccia, which can be described by two endmembers: sheared eclogite breccia composed of a strongly sheared eclogite matrix containing preserved granulite blocks and unsheared eclogite breccia, where the eclogite matrix was not subjected to pervasive ductile deformation (50-90 % eclogite). Ultimately, shear zones evolve that are up to a few hundred meters thick and are almost entirely composed of eclogite with little to no preserved granulite (>90 % eclogite).

3. Model Setup

The aim of this study is to obtain effective P wave velocities and the corresponding P wave anisotropy from variably eclogitized lower crustal rocks based on observed 2D geometric arrangements that act as an effective medium. Both the effective medium and the individual rock

types are treated as linear elastic anisotropic material for which Hooke's law gives the relationship between stress (σ_{ij}) and strain (ε_{kl}):

$$\sigma_{ij} = c_{ijkl}\,\varepsilon_{kl}$$

In 2D the 2x2x2x2 elastic tensor, which we represent by a symmetric 3-by-3 matrix in Voigt notation (using the mapping 11→1, 22→2 and 12→3), is sufficient to fully describe the in-plane anisotropy:

$$\begin{bmatrix} c_{11} & c_{12} & c_{13} \\ c_{21} & c_{22} & c_{23} \\ c_{31} & c_{32} & c_{33} \end{bmatrix}$$

Due to symmetry considerations c_{13}, c_{23}, c_{31}, and c_{32} are expected to be zero, and c_{12} should be equal to c_{21}. One way of obtaining the effective properties is to run numerical experiments solving the elasto-dynamic wave equations and recording the time necessary for a wave to travel through the medium (e.g., Saenger et al., 2004). Alternatively, we calculate the P wave velocities from the elastic tensor of the effective medium using the formulas for transversely isotropic media (Mavko et al., 2009):

$$V_P = \left(c_{11}\sin^2\theta + c_{22}\cos^2\theta + c_{33} + \sqrt{M}\right)^{\frac{1}{2}}(2\rho)^{-1/2}$$

where:

$$M = [(c_{11} - c_{33})\sin^2\theta - (c_{22} - c_{33})\cos^2\theta]^2 + (c_{12} - c_{33})^2\sin^2 2\theta$$

The individual components of the 2D elastic tensor (c_{ijkl}) of the effective medium are calculated from the stresses and strains calculated in a set of numerical experiments. For this purpose, three experiments (Fig. 3) are performed for each geometric model, applying different boundary conditions: (1) The area of interest is compressed along the y axis along the upper and lower boundary by imposing a fixed displacement. Along the left and right boundary displacement in x direction is zero. (2) The medium is compressed horizontally, that is, along the x axis. In this

case displacement in y direction is zero along the top and bottom boundary. (3) Finally, simple shear is enforced along the top and bottom boundary, that is, displacement to the right along the top boundary and to the left at the bottom boundary, resulting in shear parallel to the x axis. A fourth experiment (simple shear parallel to the y axis) was used for validation and yielded the same results as experiment (3), as is required from the symmetry of the elasticity tensor.

The three experiments result in a set of nine equations for six unknown components of the stress tensor, so only 6 of these equations are needed. Due to the setup of each experiment specific strains are zero which allows to simplify the equations to:

$$c_{21} = \frac{\sigma_{xx}}{\varepsilon_{yy}},\ c_{22} = \frac{\sigma_{yy}}{\varepsilon_{yy}}\text{, and } c_{23} = \frac{\sigma_{xy}}{\varepsilon_{yy}}$$

for experiment 1,

$$c_{11} = \frac{\sigma_{xx}}{\varepsilon_{xx}},\ c_{12} = \frac{\sigma_{yy}}{\varepsilon_{xx}}\text{, and } c_{13} = \frac{\sigma_{xy}}{\varepsilon_{xx}}$$

for experiment 2, and

$$c_{31} = \frac{\sigma_{xx}}{\varepsilon_{xy}},\ c_{32} = \frac{\sigma_{yy}}{\varepsilon_{xy}}\text{, and } c_{33} = \frac{\sigma_{xy}}{\varepsilon_{xy}}$$

for experiment 3.

To extract the elastic properties of the effective medium, strain (ε_{kl}) and stress (σ_{ij}) are averaged along the appropriate boundary. During vertical compression (experiment 1) strain and stress are averaged along the top and bottom boundary giving the components of the elastic tensor that describe the properties of the effective medium in y direction (c_{21}, c_{22}, and c_{23}). Equivalently, strain and stress are averaged at the left and right boundary during horizontal compression (experiment 2), giving the components of the elastic tensor describing the x direction (c_{11}, c_{12}, and c_{23}). Finally, during the simple shear experiment strain and stress at the top and bottom boundary are averaged giving the remaining components of the elastic tensor (c_{31}, c_{32}, and c_{33}). The boundaries at which the displacement for each of the experiments is enforced are kept far

211 away from the medium of interest to avoid boundary effects. Strain and stress are then averaged
212 along the inner boundary surrounding only the medium of interest (red in Fig. 3). In those
213 examples modelling the P wave velocities of the small-scale shear zones and the small-scale
214 static overprint the eclogite is in contact with the inner boundary in some cases. Here the eclogite
215 was extended into the area between inner and outer boundary to avoid edge effects.
216 The P wave velocities of the effective medium can then be calculated from the resulting 2D
217 elastic tensor. Bulk density is obtained by calculating the mean of the densities weighted by the
218 area of the granulite and eclogite used for the calculation. Note that the 2D elastic tensor is not
219 sufficient to adequately describe S wave velocities because it does not describe the material
220 properties for an S wave polarized perpendicular to the plane.
221 The calculations are performed, using the finite element method (FEM), employing an irregular
222 triangular grid. Meshing is done using the mesh generator triangle (Shewchuk, 1996). Each
223 triangular element consists of six nodes in which the displacement field is calculated and
224 interpolation between the nodes is quadratic.
225 The method of obtaining the P wave velocity described above was tested and benchmarked using
226 a layered medium, a problem for which an analytical solution exists (Backus, 1962), and
227 resulting P wave velocities were, within 0.5% error, those calculated from the analytical solution.
228 The physical properties for each element representing the different material are given by the
229 elastic tensor of the corresponding lithology, i.e., granulite or eclogite. Representative elastic
230 tensors were calculated from the velocity measurements (x-z plane) in Zertani et al. (2019a).
231 From this data, each component can be calculated separately with the exception of C_{12}, as this
232 would require information on the variation of elastic wave speeds along oblique directions not
233 available from laboratory measurements. Therefore, we simply used the mean P wave velocity

234 between the x and z axis to approximate the velocity of a P wave travelling at a 45° angle to the
235 foliation. In order to test the relative influence of the intrinsic properties of the constituting
236 lithologies and the geometries themselves, we used two different eclogites and two different
237 granulites (Tab. 1). Because the eclogites measured by Zertani et al. (2019a) were all collected
238 from the main shear zones exposed on Holsnøy, they all have a high P wave anisotropy. In order
239 to estimate effective properties for statically eclogitized areas, where the eclogite would likely
240 have a lower initial anisotropy, we assumed a lower velocity in x direction for one of the samples
241 (N-101 in Zertani et al., 2019a), thus giving a lower P wave anisotropy of 4%, which is in
242 accordance with others reported from Holsnøy (Fountain et al., 1994). Specifically, we chose to
243 use the velocity measured at lower confining pressure (600 MPa). This way, while the velocity is
244 artificially reduced it is still a function of the existing mineral assemblage.

245 **Tab. 1. Seismic velocities of the eclogites and granulites used for the FE calculations. The velocities**
246 **(V_P and V_S), densities and anisotropies were taken from Zertani et al. (2019a). The star indicates**
247 **that V_{PX} of N-101 was adjusted so that an anisotropy of 4% results (see text). Anisotropy was**
248 **calculated as $100*(V_{PX}-V_{PY})/V_{Pmean}$. Velocities (V) are given in km s^{-1}, density (ρ) in kg m^{-3} and**
249 **anisotropy (A) in %.**

	eclogite		granulite	
Sample	N-059	N-101	N-058A	N-103
V_{PX}	8.45	8.31*	7.12	7.76
V_{PZ}	7.74	8.01	6.99	7.46
V_{S1}	4.58	4.65	3.75	4.12
V_{S2}	4.70	4.64	3.77	4.24
ρ	3296	3483	2833	3139
A_{VP}	9	4	2	4

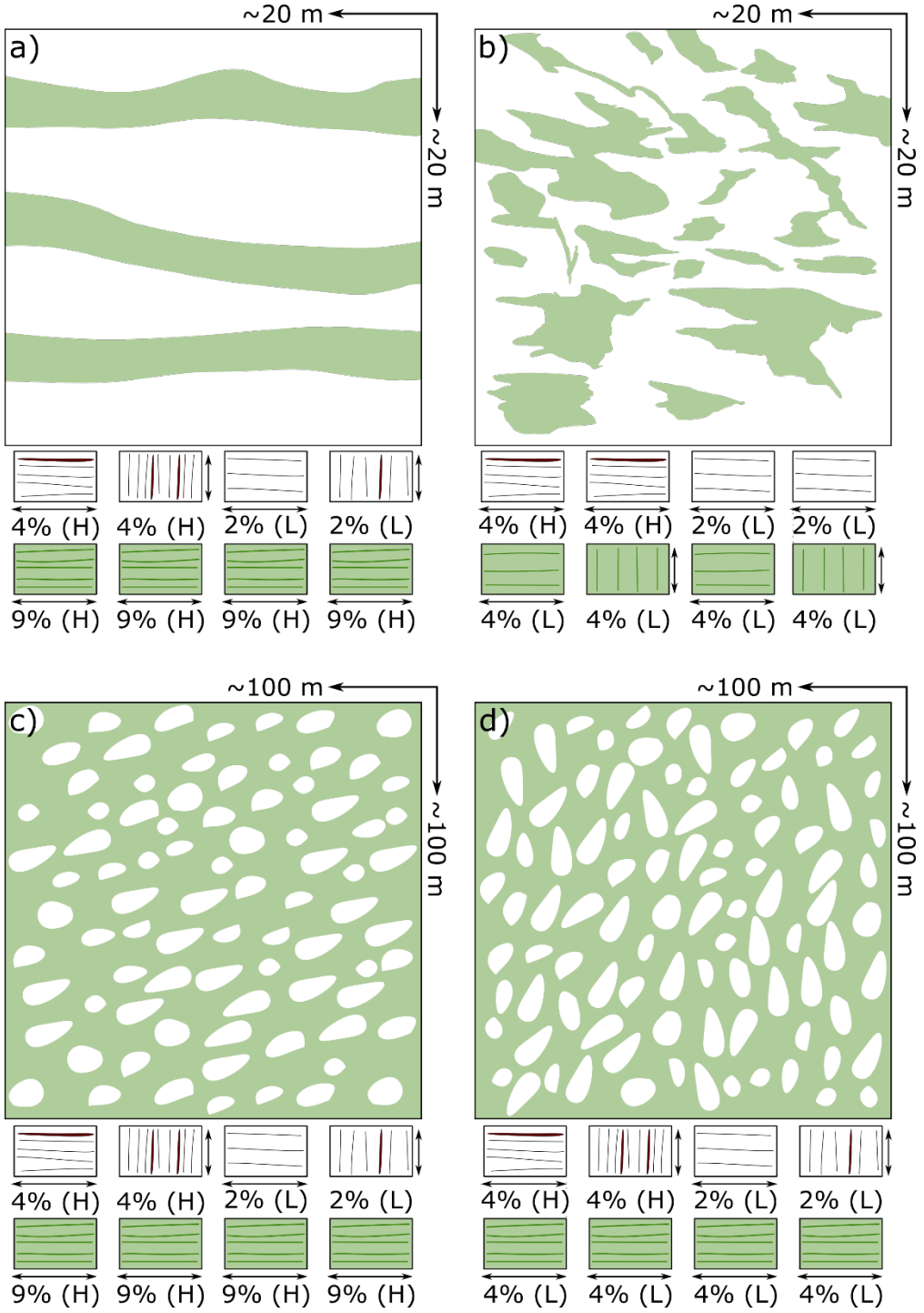

Fig. 2. Examples of the geometries used for the FEM calculations. Eclogite is shown in green and granulite in white. (a) Small-scale eclogite facies shear zones representative of an area of ~20-by-20 m. The example shown here contains ~30% eclogite. For the calculations with other eclogite abundances the thickness of the shear zone was varied accordingly. (b) Small-scale static eclogite overprint representative of an area of ~20-by-20 m. The example shown here contains ~30% eclogite. For calculations with other eclogite abundances the size of the eclogite patches was varied accordingly. (c) Sheared eclogite breccia with regularily oriented granulite blocks. The example is

representative of an area of ~100-by-100 m and ~70% eclogite. The size of the granulite blocks remains the same throughout all calculations. To perform calculations with different eclogite abundances the abundance of granulite blocks was altered. (d) Unsheared eclogite breccia with the same variations as in (c). Below each image the corresponding properties of eclogite and granulite used for the calculations are given. Each column represents one model series. The percentage gives the strength of the P wave anisotropy of the corresponding rock and the arrow gives the orientation of the fast P wave direction used for the calculations. L and H indicate whether the higher or lower-anisotropy version was used.

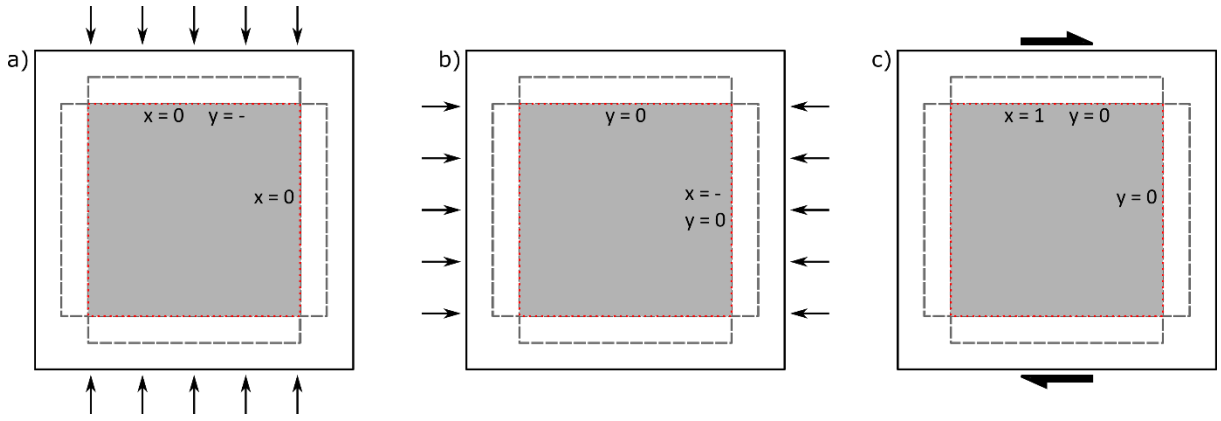

Fig. 3. Illustration of the three experiments with varying boundary conditions conducted for each computation; (a) Vertical compression, (b) horizontal compression, and (c) horizontal simple shear. The grey area represents the medium for which the properties are modelled. The red dotted square represents the boundaries at which the results are extracted and the grey dashed lines represents the area in which structures were extended if they are in direct contact with the boundary (see text for details).

Tab. 2. Resulting minimum and maximum P wave velocities and P wave anisotropy for each of the calculated models. Velocities are given in km s^{-1} and anisotropy is given in %. For each model the properties of the granulite and eclogite used for the calculation is indicated with the following scheme; L: low-anisotropy, H: high-anisotropy, X: fast axis is oriented horizontally, and Y: fast axis is oriented vertically.

Structural Association	Eclogite		Granulite		Vp_{min}	Vp_{max}	A	Vp_{min}	Vp_{max}	A	Vp_{min}	Vp_{max}	A	Vp_{min}	Vp_{max}	A
eclogite abundance [%]					11.1			21.9			30.7			39.3		
Granulite with small scale shear zones	H	X	H	X	7.49	7.84	4.6	7.51	7.91	5.2	7.54	7.97	5.7	7.56	8.04	6.1
	H	X	H	Y	7.58	7.76	2.3	7.66	7.75	1.2	7.70	7.77	1.0	7.72	7.86	1.8
	H	X	L	X	7.04	7.29	3.5	7.10	7.45	5.6	7.15	7.56	5.6	7.20	7.68	6.5
	H	X	L	Y	7.15	7.18	0.5	7.21	7.35	2.0	7.25	7.48	3.1	7.29	7.61	4.3
eclogite abundance [%]					10.9			20.0			31.9			38.2		
Granulite with static eclogitization	L	X	H	X	7.51	7.81	3.9	7.55	7.85	4.0	7.60	7.91	4.1	7.62	7.94	4.2
	L	Y	H	X	7.53	7.78	3.2	7.59	7.80	2.7	7.67	7.82	1.9	7.72	7.84	1.6
	L	X	L	X	7.06	7.21	2.1	7.12	7.30	2.5	7.20	7.43	3.1	7.24	7.52	3.8
	L	Y	L	X	7.08	7.19	1.4	7.15	7.25	1.3	7.25	7.35	1.2	7.30	7.41	1.5
eclogite abundance [%]					53.1			63.3			75.1			81.7		
Sheared eclogite breccia	H	X	H	X	7.61	8.13	6.6	7.64	8.20	7.1	7.67	8.27	7.6	7.69	8.32	7.9
	H	X	H	Y	7.75	7.99	3.0	7.75	8.08	4.2	7.75	8.19	5.6	7.74	8.26	6.5
	H	X	L	X	7.38	7.83	6.0	7.45	7.96	6.7	7.53	8.10	7.3	7.58	8.19	7.8
	H	X	L	Y	7.44	7.77	4.3	7.50	7.91	5.3	7.57	8.06	6.4	7.61	8.17	7.1
eclogite abundance [%]					52.6			63.3			70.9			81.7		
Unsheared eclogite breccia	L	X	H	X	7.77	8.06	3.7	7.82	8.11	3.7	7.86	8.15	3.6	7.91	8.20	3.7
	L	X	H	Y	7.90	7.91	0.1	7.93	7.99	0.7	7.95	8.05	1.3	7.97	8.14	2.1
	L	X	L	X	7.54	7.71	2.3	7.63	7.83	2.5	7.72	7.92	2.5	7.81	8.05	3.0
	L	X	L	Y	7.60	7.65	0.6	7.68	7.77	1.1	7.76	7.87	1.4	7.84	8.01	2.2

Structural Association	Eclogite		Granulite		Vp_{min}	Vp_{max}	A
eclogite abundance [%]					47.9		
Granulite with small scale shear zones	H	X	H	X	7.58	8.10	6.6
	H	X	H	Y	7.74	7.95	2.7
	H	X	L	X	7.26	7.80	7.1
	H	X	L	Y	7.34	7.74	5.2
eclogite abundance [%]					47.5		
Granulite with static eclogitization	L	X	H	X	7.67	8.00	4.2
	L	Y	H	X	7.79	7.86	0.9
	L	X	L	X	7.32	7.63	4.2
	L	Y	L	X	7.38	7.49	1.5
eclogite abundance [%]					89.2		
Sheared eclogite breccia	H	X	H	X	7.71	8.37	8.3
	H	X	H	Y	7.74	8.34	7.4
	H	X	L	X	7.65	8.30	8.2
	H	X	L	Y	7.66	8.28	7.7
eclogite abundance [%]					90.3		
Unsheared eclogite breccia	L	X	H	X	7.96	8.25	3.6
	L	X	H	Y	7.99	8.22	2.8
	L	X	L	X	7.91	8.16	3.2
	L	X	L	Y	7.92	8.15	2.8

280

4. Results

In order to approximate bulk P wave velocities and anisotropy of the structural associations on Holsnøy we calculate the properties of the effective medium of exemplary geometries with varying attributes (Fig. 2). These geometries are constructed based on field observations from Zertani et al. (2019b). The panels in Fig. 2 correspond to each of the endmembers distinguished in Zertani et al. (2019b). We then systematically vary the main configurations that can be observed in the field. These are: a) amount of eclogites, b) orientation of the main foliation or the constituting lithologies, and c) strength of the deformation fabric in the individual lithologies, mainly considering if the eclogites were dominated by static or dynamic eclogitization. Granulites with small-scale shear zones and granulites with small-scale static eclogitization features are each calculated with eclogite abundances between ~10 and ~50% and the sheared and unsheared eclogite breccia are calculated with eclogite abundances between ~50 and ~90%. Additionally, the orientation of the fast and slow axis of granulites and eclogites is varied so that the anisotropy of the constituting lithologies is either parallel or perpendicular to each other. Fig. 2 and Tab. 2 summarize the orientations used for each calculation as well as the rock properties of the eclogites and granulites implemented in the models.

4.1 P wave velocity and anisotropy of small-scale eclogitization features

The process of eclogitization, as it can be studied on Holsnøy, is driven by two contrasting endmember mechanisms: eclogitization proceeding along shear zones (Fig. 2a) or developing as a static overprint (Fig. 2b). In the first type, eclogitization proceeds along shear zones that widen progressively with time (Austrheim, 1987). Thus, we calculated P wave velocities for 20 examples with varying shear zone thickness as well as varying elastic properties of the eclogite and granulite implemented in the models (see Fig. 2, Tab. 2 for details).

Comparing all models shows that the calculated P wave velocities with higher-anisotropy (stronger deformation fabric) granulites are, in general, higher than those with lower-anisotropy granulites. Furthermore, with increasing shear zone thickness (i.e., amount of eclogite), the P wave velocity in both the slow and the fast P wave direction increases linearly (Tab. 2; Fig. 4a). The one exception to this trend is given by the models that feature both higher-anisotropy eclogite and the higher-anisotropy granulite, with the fast axis of both rocks oriented perpendicular to each other: the fast axis of the eclogite parallel to the shear zones and the fast axis of the granulite perpendicular to them. For this geometry, the resulting P wave velocities for the fast and slow axis of the effective medium converge up to an eclogite abundance of ~30% and then diverge toward higher eclogite abundance. This coincides with a change of the orientations of the fast and slow direction. In this scenario, the velocity perpendicular to the shear zones is almost constant. The velocity parallel to the shear zones, however, increases significantly from 7.58 to 7.95 km s^{-1} with increasing eclogite abundance. The fast axis is thus perpendicular to the shear zones for an eclogite abundance <30% and parallel to the shear zones from ~30–50% eclogite abundance. The orientation of the slow direction rotates progressively in the other direction. In all other model sequences, the fast direction is parallel to the shear zones and the slow direction is perpendicular.

The corresponding P wave anisotropy also increases with increasing shear zone thickness and reaches a maximum value of 7.1% (Fig. 5). In most models, this increase is near-linear with increasing eclogite abundance. In contrast, the resulting P wave anisotropy of those calculations featuring a higher-anisotropy granulite with the fast axis oriented perpendicular to the shear zone decreases between ~10% and ~30% eclogite abundance and then increases until ~50% eclogite

abundance. Finally, the P wave anisotropy at ~50% eclogite abundance returns to approximately the same value of ~2-3%, as the P wave anisotropy at ~10% eclogite abundance.

In general, the resulting P wave anisotropy is larger when the fast axes of both granulite and eclogite are oriented parallel to the shear zone, compared to those examples where the fast axis of the granulite is oriented perpendicular to the shear zone. At lower eclogite abundance the calculations implementing a higher-anisotropy granulite result in a higher anisotropy of the effective medium, while the results at higher eclogite abundance indicate that the anisotropy of the effective medium is higher if the granulite has a lower intrinsic anisotropy (Fig. 5).

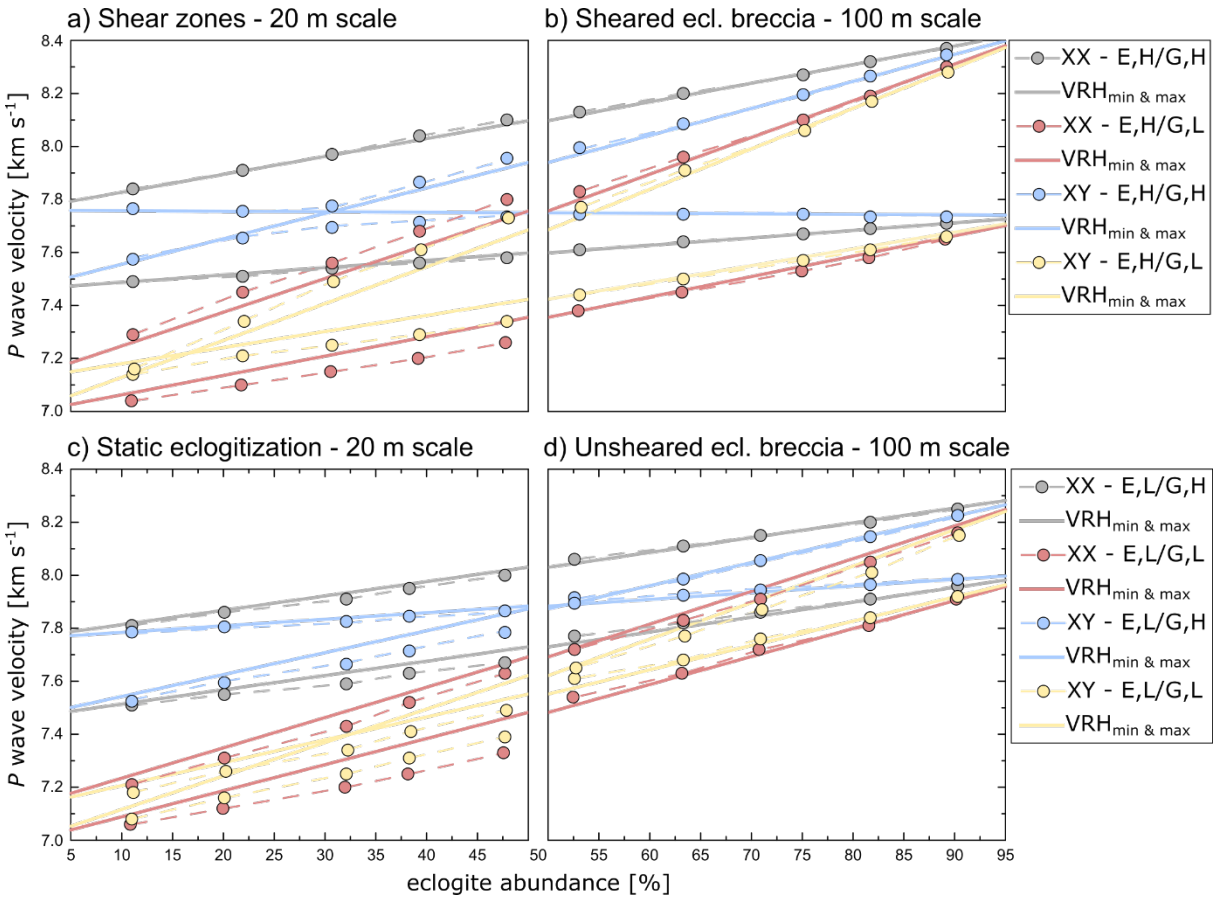

Fig. 4. P wave velocities of the FEM calculations: (a) Small-scale eclogite shear zones, (b) sheared eclogite breccia, (c) small-scale static eclogite, and (d) unsheared eclogite breccia. The legend for (a) and (b) is to the right of (b) and the legend for (c) and (d) is to the right of (d). Each model series is shown by two connecting dashed lines. The upper line represents the maximum velocities and the lower line represents the minimum velocities. The legend is given in the following scheme; XX: fast axis of granulite and eclogite are parallel, XY: fast axis of granulite and eclogite are perpendicular,

E,H or E,L: eclogite with high anisotropy or low anisotropy, respectively, G,H or G,L: granulite with high or low anisotropy, respectively. Solid lines indicate Voigt-Reuss-Hill averages in the same color scheme as the modeling results averaged from the input velocities in x and y direction, respectively, thus giving minimum and maximum bounds.

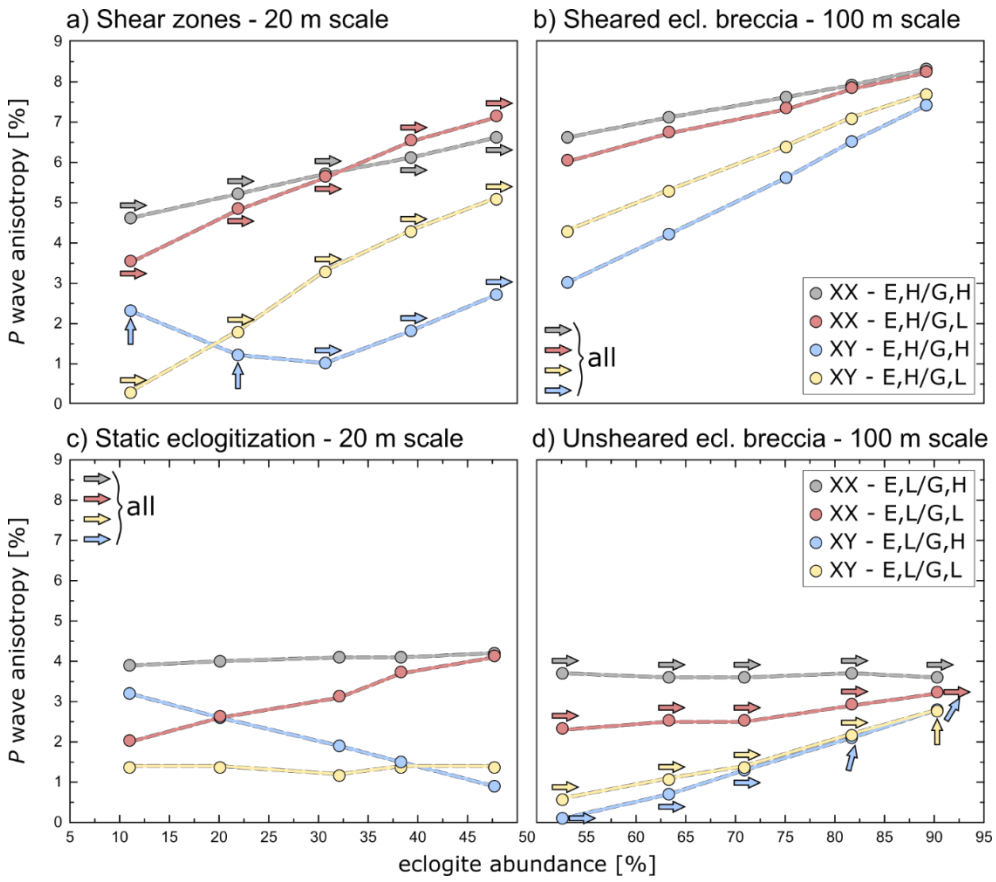

Fig. 5. P wave anisotropy of the FEM calculations: (a) Small-scale eclogite shear zones, (b) sheared eclogite breccia, (c) small-scale static eclogite, and (d) unsheared eclogite breccia. For a description of model types and explanation of the legend, refer to Fig. 4. Arrows indicate the direction of the fast axis of the effective medium with horizontal being in x direction and vertical in y direction.

Additionally, eclogitization on Holsnøy also proceeded statically without significant ductile deformation (Jamtveit et al., 2000; Zertani et al., 2019b). Here, eclogitization most commonly advances parallel to the granulite foliation. For this case, we again calculated 20 different examples, varying both the abundance of eclogite and the elastic properties of the granulite and the eclogite (Fig. 2b; Tab. 2).

The resulting P wave velocities show a similar trend as those from the examples featuring small-scale shear zones. Both the velocity of the fast and the slow axes increase linearly with increasing abundance of eclogite (Fig. 4c). Further, the models featuring granulites with higher anisotropy result in faster P wave velocities of the effective medium than the models implementing lower-anisotropy granulites. Additionally, the P wave velocities are in the same range as the ones calculated for small-scale shear zones.

The orientations of the fast and slow axes are typically constant with the fast axis being parallel to the granulite foliation (horizontal) and the slow axis perpendicular. Only in the calculations where the lower-anisotropy eclogite and granulite with the orientation of the fast axes perpendicular to each other are implemented, the resulting orientation changes slightly. These calculations indicate that the fast axis remains horizontal (i.e., parallel to the granulite foliation) while the slow axis rotates slightly away from the initial vertical orientation.

The P wave anisotropy shows a variable trend comparing the different models. The medium featuring the higher-anisotropy granulite, with both the fast axes of the granulite and eclogite oriented parallel to each other result in a P wave anisotropy of ~4% that essentially does not change with varying eclogite abundance (Fig. 5d). The same is observed for the models featuring the lower-anisotropy granulite with the fast axes of the granulite and eclogite being oriented perpendicular to each other. Here, the resulting P wave velocity remains relatively constant around 1–2%.

In contrast, the resulting anisotropy of the other two model types changes with increasing eclogite abundance. The sequence featuring a lower-anisotropy granulite with the fast axis oriented parallel to the fast axis of the eclogite increases from ~2% to ~4%, while the sequence

379 featuring the higher-anisotropy granulite with the fast axes of the two rocks oriented
380 perpendicular to each other decreases from ~3% to <1%.

381 4.2 P-wave velocity of eclogite breccia

382 With increasing degree of eclogitization the so-called eclogite breccia develops, which is
383 composed of an eclogite matrix that surrounds preserved blocks of granulite (Boundy et al.,
384 1992). On Holsnøy, the eclogite breccia can be divided into two endmember types (Zertani et al.,
385 2019b): The sheared eclogite breccia is characterized by a strongly sheared and foliated eclogite
386 matrix, while the matrix of the unsheared eclogite breccia is diffuse and less foliated.
387 We calculated 20 examples for each of the two types, varying the abundance of eclogite and the
388 elastic properties of the granulite and eclogite (see Fig. 2c, d; Tab. 2). For all examples of the
389 sheared eclogite breccia, the P wave velocities increase linearly with increasing eclogite
390 abundance. All fast axes and all slow axes converge toward higher eclogite abundances, thus
391 giving fairly distinct maximum and minimum P wave velocities at high eclogite abundances that
392 are independent of the elastic properties of the granulite implemented in the model. (Fig. 4; Fig. 5).
393 The slope of the linear increase for the different models is similar to the models dealing with
394 small-scale shear zones. Further, the fast axis of the effective medium in all models is parallel to
395 the shear plane (horizontal) and the slow axis is perpendicular. Additionally, the P wave
396 velocities at ~50% eclogite abundance agree well between the models for small-scale shear zones
397 and the sheared eclogite breccia at the same eclogite fraction.
398 As in the case of the small-scale shear zones, the P wave anisotropy calculated for the sheared
399 eclogite breccia increases nearly linearly with increasing eclogite abundance reaching 7–9% at
400 ~90%. Further, P wave anisotropy is consistently higher for models where the fast axes of the
401 granulite and the eclogite are oriented parallel. In this scenario the anisotropy reaches its

maximum when both the granulite and the eclogite have a high anisotropy. If the fast axis of the granulite, however, is perpendicular to the fast axis of the eclogite, the resulting anisotropy is higher when the implemented granulite has a lower anisotropy.

The P wave velocities calculated for the unsheared eclogite breccia show the same general trends as those for the sheared eclogite breccia (Fig. 4d). The only deviation results from the examples implementing granulite and eclogite with their anisotropy perpendicular to each other. Here the calculations result in a change of the orientation at high eclogite abundances.

The trends of the P wave anisotropy of the unsheared eclogite breccia in all calculated examples is lower than the comparable examples of the sheared eclogite breccia (Fig. 5). Most sequences, however, also slightly increase with increasing eclogite abundance, except for those where a lower-anisotropy eclogite is paired with the higher-anisotropy granulite, both of which have their fast axes parallel to each other. In that case the P wave anisotropy is nearly constant at ~3.7% (Tab. 2).

5. Discussion

Many studies have calculated or measured P wave velocities of various metamorphic rocks with the aim of interpreting the results of large-scale geophysical imaging techniques (e.g., Almqvist & Mainprice, 2017). However, the sample sizes used for these interpretations are typically far below the resolution of geophysical studies. It is thus essential to understand how geometries formed at depth during ongoing eclogitization shape the seismic properties of the effective medium in combination with the (anisotropic) seismic properties of the constituent rocks.

5.1 Effective properties of 20 m and 100 m scale structures

Essentially, the P wave velocities calculated for the different geometrical setups show that the velocities are controlled by the velocities of the constituent rocks and their proportions (Fig. 4,

Fig. 5). This has been accepted and applied by previous studies by calculating, for example, Voigt-Reuss-Hill (VRH) averages (Hill, 1952) and linking those with the crystallographic preferred orientations of the mineral phases (e.g., Hacker et al., 2014; Llana-Funez & Brown, 2012; Worthington et al., 2013). Most of these studies, however, obtain information from the thin section scale to recognize crustal-scale processes or to interpret the results from large-scale geophysical imaging studies. The results presented in this study indicate that Voigt-Reuss-Hill averages calculated from outcrop-scale features are sufficiently precise to estimate the effective properties on a variety of scales (Fig. 4). Essentially, the geometries that are representative of eclogitization of crustal rocks have only limited influence on the resulting P wave velocities. Only in isolated cases the velocities are modified, thus deviating from the calculated VRH averages (Fig. 4a and 4c). Here a minor geometric effect is plausible, however, this effect results in a maximum modification of <0.2 km s^{-1} of the P wave velocity and is thus negligible in the context of large-scale crustal processes.

However, P wave anisotropy varies between the different geometrical configurations (Fig. 5). Here, we distinguish two contributing factors in order to characterize their influence separately. (1) The configuration that the different lithologies have to one another on the outcrop scale or larger. This includes, for example, eclogite shear zones that crosscut granulites. In the following this factor will be termed external geometry as it involves the relationship of the lithologies to each other but not specifically the properties of the constituting lithologies themselves. (2) The second contributing geometrical factor will be termed internal geometry in the following. It highlights the properties of the lithologies themselves by characterizing the relationship between the directional dependence of the elastic properties of the different lithologies that is caused by, for example, crystallographic preferred orientations or shape preferred orientations. The internal

geometry thus distinguishes whether the fastest velocity of the eclogite and granulite are parallel or oblique to each other.

Our results reveal the importance of the internal geometry compared to that of the external geometry (Fig. 4, Fig. 5). As discussed above, the external geometry only has a minor effect on the P wave velocities and anisotropy of the effective medium. The variation of anisotropy for the different configurations tested by us are thus controlled by the internal geometry. The most important factor is the anisotropy of the constituent lithologies that are necessary to produce significant anisotropy of the effective medium. Additionally, the effective anisotropy is strengthened or weakened by the relationship of the individual anisotropies of the lithologies. Anisotropies are higher if the fast axes of the lithologies are aligned but not higher than the highest contributing anisotropy (Fig. 5). Further, our results demonstrate the predominance of the higher anisotropy lithology and suggest that the fast axis of the effective medium is parallel to the anisotropy of the matrix lithology (i.e., in line with the fabric of granulite or eclogite), if the difference in anisotropy between the lithologies is small, or the higher anisotropy lithology, even if this lithology is less abundant (Fig. 5); meaning a strongly deformed rock, such as eclogite in shear zones, controls the overall anisotropy even at low abundances.

5.2 Effective properties on the kilometer scale

Combining our results with field observations provides the opportunity to understand how partial eclogitization of crustal rocks alters the seismic properties on a scale significantly larger than what can be measured in the laboratory. Our results suggest that P wave velocities are almost entirely controlled by the velocities and abundances of the constituting rocks (Fig. 4). Essentially, there is no difference in the P wave velocities between rocks that have formed through static eclogitization and those that formed associated with ductile deformation. Neither the finite

geometries nor the intrinsic seismic anisotropy of the granulites and eclogites have a significant impact on the resulting bulk velocities and the variations that can be distinguished are minor. The P wave anisotropy, however, is influenced strongly by the anisotropy of the rocks that make up the effective medium (Fig. 5). Further, our results show that the rock with the higher anisotropy controls bulk anisotropy. In any case, the exemplary geometries discussed above are still far smaller than what can be resolved with large-scale geophysical methods.

Therefore, we used these results to extract bulk properties of the effective medium at a scale that could be resolved by large-scale geophysical imaging (Fig. 6). Accordingly, we used an area on Holsnøy that is ~3.9-by-4.6 km in size (Fig. 1 and Fig. 6a), and provides a coherent natural laboratory for eclogitization related structures. The geometries are based on the map shown in Zertani et al. (2019b). As properties for the different map units we implemented the resulting elastic tensor of the examples shown above, choosing one representative example for each of the geometric configurations, i.e., sheared eclogite breccia at ~75% eclogite with the fast axis of higher-anisotropy eclogite and higher-anisotropy granulite parallel to each other and unsheared eclogite breccia at ~71% eclogite with the fast axis of the lower-anisotropy eclogite and the higher-anisotropy granulite parallel to each other (Tab. 2). For pure eclogite and granulite we chose the higher-anisotropy versions (Tab. 1) that were also used for the calculations discussed above (Zertani et al., 2019a). The elastic tensors were rotated so that the fast axis is parallel to the structures presented by Zertani et al. (2019b).

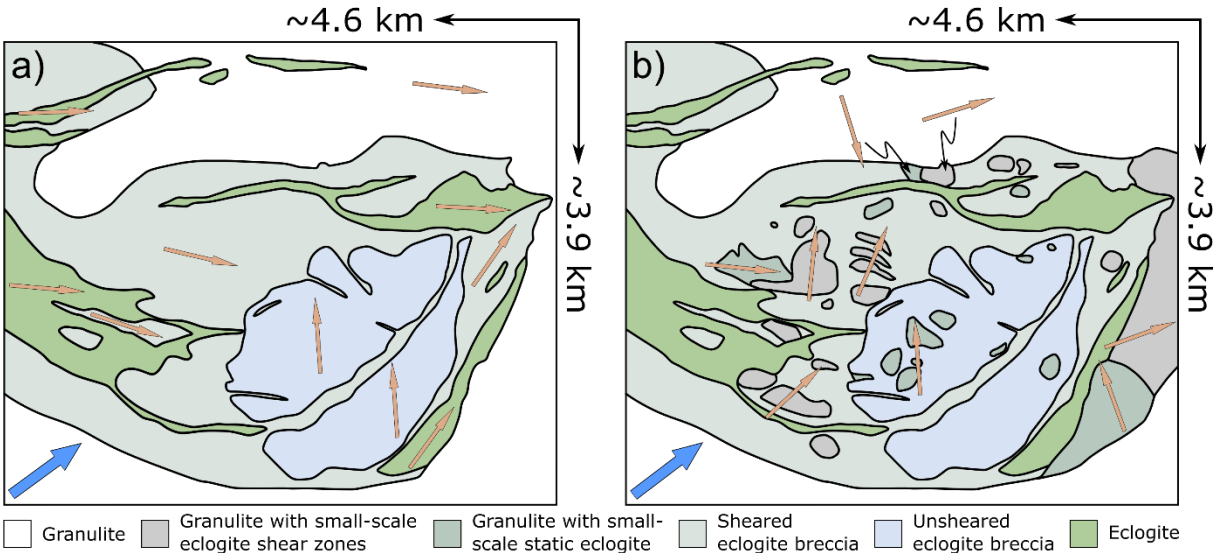

Fig. 6. Geometries used for the FEM calculations on the kilometer-scale. (a) Simpler model without smaller-scale structures. (b) More realistic model with small-scale structures. The location of this figure is given in Fig. 1. The yellow arrows indicate the direction of the fast axis implemented for the different lithologies. The blue arrows show the direction of the fastest velocity for each of the models.

Additionally, we implemented a second (more precise) model that also includes smaller-scale structures (Fig. 6b). Here we implemented the small-scale eclogite shear zones at ~31% eclogite with the lower-anisotropy granulite and the higher-anisotropy eclogite (Tab. 2) and the small-scale static eclogite occurrences at ~32% eclogite with the higher-anisotropy granulite and the lower-anisotropy eclogite (Tab. 2).

The resulting P wave velocities of both models are in the range of 8.1 km s^{-1} (fast axis) to 7.7 km s^{-1} (slow axis), i.e., within the expected range of the measured P wave velocities between granulite and eclogite (Zertani et al., 2019a). Similar velocities are also reported from geophysical studies dealing with active convergent settings, typically in the range of 7–8 km s^{-1} (e.g., Nabelek et al., 2009; Schulte-Pelkum et al., 2005; Sippl et al., 2013). Additionally, our calculation predicts a P wave anisotropy of 5.1% for the simpler model (Fig. 6a) and 4.8% for the model that includes the small-scale structures (Fig. 6b). These values are in the range of what is generally reported from higher-anisotropy eclogites and granulites (e.g., Brown et al., 2009;

Worthington et al., 2013). However, it has to be noted that the anisotropy presented here is representative for the effective medium on a kilometer-scale and not only for single (handspecimen-sized) samples.

5.3 Implications for imaging of continental collision

P wave velocities below the Tibetan plateau are suggested to be >7.0 km s^{-1}, which was interpreted to represent ~30% eclogitization (Schulte-Pelkum et al., 2005) . Our calculation for Holsnøy is representative of ~50% eclogitization and yields slightly higher velocities. It thus seems possible to estimate the degree of eclogitization based on P wave velocities. However, this is only feasible if the backazimuthal distribution is sufficiently representative (Nabelek et al., 2009; Schulte-Pelkum et al., 2005).

The retrieved P wave anisotropy of ~5% from our model is sufficiently high that it could result in a backazimuthal dependence of the retrieved signal in seismological studies. Additionally, our calculations of P wave anisotropy of the different structural associations that could be expected in a partially eclogitized crust show how different geometries can cause high P-wave anisotropy (Fig. 5). A typical example of an active setting where the rocks at depth are presumably similar to those on Holsnøy is the Himalaya-Tibet collision system, where the lower crust of India is imaged below the Himalaya (Jackson et al., 2004; Labrousse et al., 2010). Using the receiver function method, it has been shown that the retrieved signal of the Moho is sharp using earthquakes coming from the north, while the Moho cannot be clearly imaged using earthquakes arriving from the south, suggesting an anisotropic fabric within the buried crust (Nabelek et al., 2009; Schulte-Pelkum et al., 2005). Nabelek et al. (2009) propose that this fabric is caused by the imbrication and rotation of a stratified lower crust, excluding eclogites as the cause for the anisotropy because eclogites typically have anisotropies <4%. However, our results show that

partial eclogitization of the lower crust does indeed produce high anisotropies at the scale sampled by geophysical imaging techniques. Moreover, as shown by our results the effect of external geometry on seismic anisotropy is limited suggesting that simple layering or imbrication might not produce sufficient seismic anisotropy on this scale. Our results provide an alternative explanation for the structures observed below the Himalaya. We suggest that considering the P wave velocities reported and the backazimuthal dependence (Nabelek et al., 2009; Schulte-Pelkum et al., 2005) eclogitization of the crust along ductile shear zones, similar to those exposed on Holsnøy seems the more likely explanation.

Additionally, both kilometer-scale models we present here suggest that the fast axis of the shear zone system is oriented WSW-ENE. At least in a qualitative sense this suggests that during ongoing eclogitization, when this anisotropy was established it was dipping toward the upper plate as is also evidenced by the top-east kinematics of the shear zone system (Jolivet et al., 2005; Raimbourg et al., 2005). Geophysical imaging suggests a northward dipping fabric within the lower Indian crust (Nabelek et al., 2009; Schulte-Pelkum et al., 2005), that is, dipping toward the Asian plate, consistent with a top to the south shear sense. Our results demonstrate that propagating eclogite-facies shear zones would produce a fabric and subsequent anisotropy with a similar orientation. The scale of those shear zones is actually a minor issue, since our results show the same dependence of effective medium properties on constitutive lithologies independent of the scale.

5.4 Implications for oceanic subduction

Although the rocks on Holsnøy originate from continental crust some implications for oceanic subduction settings can nevertheless be explored. In many geophysical studies of subducting

556 oceanic plates the descending crust is clearly imaged at shallow depth but loses its seismic signal
557 at greater depth (e.g., Bostock et al., 2002; Pearce et al., 2012; Rondenay et al., 2008; Yuan et
558 al., 2000). This decrease of the seismic signal is typically interpreted as due to a decreased
559 impedance contrast between descending crust and mantle rocks caused by eclogitization. This is
560 often accompanied by an increase of the dip angle in the Wadati-Benioff zone that indicates a
561 kink in the slab geometry (e.g., Halpaap et al., 2018; Klemd et al., 2011; Yuan et al., 2000).
562 While the subducting crust is invisible to seismological studies at this point its presence is
563 evidenced by the Wadati-Benioff zone and the inferred kink of the slab has been proposed as a
564 possible geometric obstacle that inhibits exhumation of crustal material subducted beyond that
565 point and is therefore potentially vital to understand subduction zone processes (Klemd et al.,
566 2011). Additionally, kinking on this scale must cause internal deformation of the subducting
567 slab. Whether or not this deformation is localized or homogeneously distributed and how this
568 deformation process affects ongoing eclogitization of the slab is enigmatic. However, utilizing
569 seismic anisotropy and the subsequent backazimuthal bias on the retrieved seismic signal might
570 prove a powerful tool to unravel these processes in active subduction zones. In this context,
571 although reliable imaging of the crustal anisotropy at these depths is still challenging, seismic
572 anisotropy of the subducted oceanic crust might make it possible to image it to larger depth and
573 illuminate an otherwise invisible slab.
574

575 **6. Conclusions**

576 We calculated P wave velocities and the corresponding P wave anisotropy for various
577 geometries, which are representative of partially eclogitized crust. The results show that dynamic
578 eclogitization, associated with shear zone formation, can cause a high P wave anisotropy that

579 increases with increasing eclogitization. The anisotropy of the effective medium is generally
580 controlled by the anisotropy of the matrix or by the contributing lithology that has the highest
581 anisotropy, even if this lithology is less abundant than the other contributors. Consequently,
582 patches of static eclogitization produce a comparatively low P wave anisotropy, which is in some
583 cases independent of the amount of eclogitization. The (external) geometric configuration of the
584 lithologies has little to no effect on the seismic properties of the effective medium.
585 Our results link partial eclogitization with geophysical observations at active convergent plate
586 boundaries. Previously, significant anisotropy due to eclogitization in deeply buried or subducted
587 crust has been excluded as eclogites are typically not strongly anisotropic. Contrary to this, our
588 results demonstrate that significant anisotropy due to partial eclogitization of crustal material on
589 a kilometer-scale is likely the best explanation for the discrepancy of the signals retrieved from
590 different backazimuths in seismological studies. For example, the structures seen below the
591 Himalaya are likely anisotropic due to the formation of eclogite-facies shear zones within the
592 lower Indian crust. Additionally, our results strongly encourage the utilization of seismic
593 anisotropy as a tool to visualize the structural associations at depth thus aiding the extraction of
594 the underlying mechanisms active during ongoing eclogitization of crustal material.
595

596 Acknowledgements

597 This research was supported by the Deutsche Forschungsgemeinschaft (DFG) in the framework
598 of the priority program SPP 2017 “Mountain Building in Four Dimensions (MB-4D)” by grant
599 JO 349/11-1. Funding for TBA was provided from Norges forskningsråd (NFR) project 250327.
600 Input data for the calculations are provided as figures in the supporting information and will be
601 uploaded to the OSF data repository (osf.io) after acceptance.

602

603 References

604

605

606 Almqvist, B. S. G., & Mainprice, D. (2017). Seismic properties and anisotropy of the continental
607 crust: Predictions based on mineral texture and rock microstructure. *Reviews of*
608 *Geophysics, 55*(2), 367-433. doi:https://doi.org/10.1002/2016RG000552
609 Andersen, T. B., Corfu, F., Labrousse, L., & Osmundsen, P.-T. (2012). Evidence for
610 hyperextension along the pre-Caledonian margin of Baltica. *Journal of the Geological*
611 *Society, 169*(5), 601-612. doi:https://doi.org/10.1144/0016-76492012-011
612 Austrheim, H. (1987). Eclogitization of lower crustal granulites by fluid migration through shear
613 zones. *Earth and Planetary Science Letters, 81*(2), 221-232.
614 doi:https://doi.org/10.1016/0012-821X(87)90158-0
615 Austrheim, H. (1990). The granulite-eclogite facies transition: A comparison of experimental
616 work and a natural occurrence in the Bergen Arcs, western Norway. *Lithos, 25*(1), 163-
617 169. doi:https://doi.org/10.1016/0024-4937(90)90012-P
618 Austrheim, H. (1991). Eclogite formation and dynamics of crustal roots under continental
619 collision zones. *Terra Nova, 3*(5), 492-499. doi:https://doi.org/10.1111/j.1365-
620 3121.1991.tb00184.x
621 Austrheim, H., & Griffin, W. L. (1985). Shear deformation and eclogite formation within
622 granulite-facies anorthosites of the Bergen Arcs, western Norway. *Chemical Geology,*
623 *50*(1), 267-281. doi:https://doi.org/10.1016/0009-2541(85)90124-X
624 Backus, G. E. (1962). Long-wave elastic anisotropy produced by horizontal layering. *Journal of*
625 *Geophysical Research, 67*(11), 4427-4440. doi:10.1029/JZ067i011p04427
626 Bhowany, K., Hand, M., Clark, C., Kelsey, D. E., Reddy, S. M., Pearce, M. A., . . . Morrissey, L.
627 J. (2018). Phase equilibria modelling constraints on P–T conditions during fluid catalysed
628 conversion of granulite to eclogite in the Bergen Arcs, Norway. *Journal of Metamorphic*
629 *Geology, 36*(3), 315-342. doi:https://doi.org/10.1111/jmg.12294
630 Bloch, W., John, T., Kummerow, J., Salazar, P., Krüger, O. S., & Shapiro, S. A. (2018).
631 Watching Dehydration: Seismic Indication for Transient Fluid Pathways in the Oceanic
632 Mantle of the Subducting Nazca Slab. *Geochemistry, Geophysics, Geosystems, 19*, 3189-
633 3207. doi:https://doi.org/10.1029/2018GC007703
634 Bostock, M., Hyndman, R., Rondenay, S., & Peacock, S. (2002). An inverted continental Moho
635 and serpentinization of the forearc mantle. *Nature, 417*, 536-538.
636 doi:https://doi.org/10.1038/417536a
637 Bostock, M. G. (2013). The Moho in subduction zones. *Tectonophysics, 609*, 547-557.
638 doi:https://doi.org/10.1016/j.tecto.2012.07.007
639 Boundy, T. M., Fountain, D. M., & Austrheim, H. (1992). Structural development and
640 petrofabrics of eclogite facies shear zones, Bergen Arcs, western Norway: implications
641 for deep crustal deformational processes. *Journal of Metamorphic Geology, 10*(2), 127-
642 146. doi:https://doi.org/10.1111/j.1525-1314.1992.tb00075.x
643 Boundy, T. M., Mezger, K., & Essene, E. J. (1997). Temporal and tectonic evolution of the
644 granulite-eclogite association from the Bergen Arcs, western Norway. *Lithos, 39*(3), 159-
645 178. doi:http://dx.doi.org/10.1016/S0024-4937(96)00026-6

Brown, D., Llana-Funez, S., Carbonell, R., Alvarez-Marron, J., Marti, D., & Salisbury, M. (2009). Laboratory measurements of P-wave and S-wave velocities across a surface analog of the continental crust–mantle boundary: Cabo Ortegal, Spain. *Earth and Planetary Science Letters, 285*(1-2), 27-38. doi:https://doi.org/10.1016/j.epsl.2009.05.032

Corfu, F., Andersen, T. B., & Gasser, D. (2014). The Scandinavian Caledonides: main features, conceptual advances and critical questions. *Geological Society, London, Special Publications, 390*(1), 9-43. doi:https://doi.org/10.1144/sp390.25

Dewey, J. F., Ryan, P. D., & Andersen, T. B. (1993). Orogenic uplift and collapse, crustal thickness, fabrics and metamorphic phase changes: the role of eclogites. *Geological Society, London, Special Publications, 76*(1), 325-343. doi:https://doi.org/10.1144/GSL.SP.1993.076.01.16

Fountain, D. M., Boundy, T. M., Austrheim, H., & Rey, P. (1994). Eclogite-facies shear zones—deep crustal reflectors? *Tectonophysics, 232*(1), 411-424. doi:https://doi.org/10.1016/0040-1951(94)90100-7

Glodny, J., Kühn, A., & Austrheim, H. (2008). Geochronology of fluid-induced eclogite and amphibolite facies metamorphic reactions in a subduction–collision system, Bergen Arcs, Norway. *Contributions to Mineralogy and Petrology, 156*(1), 27-48. doi:https://doi.org/10.1007/s00410-007-0272-y

Hacker, B., Ritzwoller, M., & Xie, J. (2014). Partially melted, mica-bearing crust in Central Tibet. *Tectonics, 33*(7), 1408-1424. doi:https://doi.org/10.1002/2014TC003545

Halpaap, F., Rondenay, S., & Ottemöller, L. (2018). Seismicity, Deformation, and Metamorphism in the Western Hellenic Subduction Zone: New Constraints From Tomography. *Journal of Geophysical Research: Solid Earth, 123*(4), 3000-3026. doi:https://doi.org/10.1002/2017JB015154

Hetényi, G., Cattin, R., Brunet, F., Bollinger, L., Vergne, J., Nábělek, J. L., & Diament, M. (2007). Density distribution of the India plate beneath the Tibetan plateau: Geophysical and petrological constraints on the kinetics of lower-crustal eclogitization. *Earth and Planetary Science Letters, 264*(1-2), 226-244. doi:https://doi.org/10.1016/j.epsl.2007.09.036

Hill, R. (1952). The elastic behaviour of a crystalline aggregate. *Proceedings of the Physical Society. Section A, 65*(5), 349-354.

Hudson, J. A. (1981). Wave speeds and attenuation of elastic waves in material containing cracks. *Geophysical Journal International, 64*(1), 133-150. doi:https://doi.org/10.1111/j.1365-246X.1981.tb02662.x

Jackson, J. A., Austrheim, H., McKenzie, D., & Priestley, K. (2004). Metastability, mechanical strength, and the support of mountain belts. *Geology, 32*(7), 625-628. doi:https://doi.org/10.1130/g20397.1

Jakob, J., Andersen, T. B., & Kjøll, H. J. (2019). A review and reinterpretation of the architecture of the South and South-Central Scandinavian Caledonides—A magma-poor to magma-rich transition and the significance of the reactivation of rift inherited structures. *Earth-Science Reviews, 192*, 513-528. doi:https://doi.org/10.1016/j.earscirev.2019.01.004

Jamtveit, B., Austrheim, H., & Malthe-Sorenssen, A. (2000). Accelerated hydration of the Earth's deep crust induced by stress perturbations. *Nature, 408*(6808), 75-78. doi:https://doi.org/10.1038/35040537

Jamtveit, B., Bucher-Nurminen, K., & Austrheim, H. (1990). Fluid controlled eclogitization of granulites in deep crustal shear zones, Bergen arcs, Western Norway. *Contributions to Mineralogy and Petrology, 104*(2), 184-193. doi:https://doi.org/10.1007/bf00306442

John, T., & Schenk, V. (2003). Partial eclogitisation of gabbroic rocks in a late Precambrian subduction zone (Zambia): prograde metamorphism triggered by fluid infiltration. *Contributions to Mineralogy and Petrology, 146*(2), 174-191. doi:https://doi.org/10.1007/s00410-003-0492-8

Jolivet, L., Raimbourg, H., Labrousse, L., Avigad, D., Leroy, Y., Austrheim, H., & Andersen, T. B. (2005). Softening trigerred by eclogitization, the first step toward exhumation during continental subduction. *Earth and Planetary Science Letters, 237*(3–4), 532-547. doi:https://doi.org/10.1016/j.epsl.2005.06.047

Kern, H., Gao, S., & Liu, Q.-S. (1996). Seismic properties and densities of middle and lower crustal rocks exposed along the North China Geoscience Transect. *Earth and Planetary Science Letters, 139*(3), 439-455. doi:https://doi.org/10.1016/0012-821X(95)00240-D

Kim, D., Keranen, K. M., Abers, G. A., & Brown, L. D. (2019). Enhanced Resolution of the Subducting Plate Interface in Central Alaska From Autocorrelation of Local Earthquake Coda. *Journal of Geophysical Research: Solid Earth, 124*(2), 1583-1600. doi:https://doi.org/10.1029/2018jb016167

Kind, R., Yuan, X., & Kumar, P. (2012). Seismic receiver functions and the lithosphere–asthenosphere boundary. *Tectonophysics, 536-537*, 25-43. doi:https://doi.org/10.1016/j.tecto.2012.03.005

Klemd, R., John, T., Scherer, E. E., Rondenay, S., & Gao, J. (2011). Changes in dip of subducted slabs at depth: Petrological and geochronological evidence from HP–UHP rocks (Tianshan, NW-China). *Earth and Planetary Science Letters, 310*(1-2), 9-20. doi:https://doi.org/10.1016/j.epsl.2011.07.022

Labrousse, L., Hetényi, G., Raimbourg, H., Jolivet, L., & Andersen, T. B. (2010). Initiation of crustal-scale thrusts triggered by metamorphic reactions at depth: Insights from a comparison between the Himalayas and Scandinavian Caledonides. *Tectonics, 29*(5), TC5002. doi:https://doi.org/10.1029/2009TC002602

Llana-Funez, S., & Brown, D. (2012). Contribution of crystallographic preferred orientation to seismic anisotropy across a surface analog of the continental Moho at Cabo Ortegal, Spain. *Geological Society of America Bulletin, 124*(9-10), 1495-1513. doi:https://doi.org/10.1130/b30568.1

Mavko, G., Mukerji, T., & Dvorkin, J. (2009). *The rock physics handbook: Tools for seismic analysis of porous media*: Cambridge university press.

Nabelek, J., Hetenyi, G., Vergne, J., Sapkota, S., Kafle, B., Jiang, M., . . . Hi, C. T. (2009). Underplating in the Himalaya-Tibet collision zone revealed by the Hi-CLIMB experiment. *Science, 325*(5946), 1371-1374. doi:https://doi.org/10.1126/science.1167719

Pearce, F. D., Rondenay, S., Sachpazi, M., Charalampakis, M., & Royden, L. H. (2012). Seismic investigation of the transition from continental to oceanic subduction along the western Hellenic Subduction Zone. *Journal of Geophysical Research: Solid Earth, 117*, B07306. doi:https://doi.org/10.1029/2011JB009023

Raimbourg, H., Jolivet, L., Labrousse, L., Leroy, Y., & Avigad, D. (2005). Kinematics of syneclogite deformation in the Bergen Arcs, Norway: implications for exhumation mechanisms. *Geological Society, London, Special Publications, 243*(1), 175-192. doi:https://doi.org/10.1144/gsl.sp.2005.243.01.13

737 Rondenay, S., Abers, G. A., & van Keken, P. E. (2008). Seismic imaging of subduction zone
738 metamorphism. *Geology, 36*(4), 275-278. doi:https://doi.org/10.1130/G24112A.1
739 Saenger, E. H., Krüger, O. S., & Shapiro, S. A. (2004). Effective elastic properties of randomly
740 fractured soils: 3D numerical experiments. *Geophysical Prospecting, 52*(3), 183-195.
741 doi:https://doi.org/10.1111/j.1365-2478.2004.00407.x
742 Schneider, F. M., Yuan, X., Schurr, B., Mechie, J., Sippl, C., Haberland, C., . . . Negmatullaev,
743 S. (2013). Seismic imaging of subducting continental lower crust beneath the Pamir.
744 *Earth and Planetary Science Letters, 375*, 101-112.
745 doi:https://doi.org/10.1016/j.epsl.2013.05.015
746 Schulte-Pelkum, V., Monsalve, G., Sheehan, A., Pandey, M. R., Sapkota, S., Bilham, R., & Wu,
747 F. (2005). Imaging the Indian subcontinent beneath the Himalaya. *Nature, 435*(7046),
748 1222-1225. doi:https://doi.org/10.1038/nature03678
749 Shewchuk, J. R. (1996). Triangle: Engineering a 2D quality mesh generator and Delaunay
750 triangulator. In M. C. Lin & D. Manocha (Eds.), *Applied Computational Geometry*
751 *Towards Geometric Engineering* (Vol. 1148, pp. 203-222). Berlin, Heidelberg: Springer
752 Berlin Heidelberg.
753 Sippl, C., Schurr, B., Tympel, J., Angiboust, S., Mechie, J., Yuan, X., . . . Haberland, C. (2013).
754 Deep burial of Asian continental crust beneath the Pamir imaged with local earthquake
755 tomography. *Earth and Planetary Science Letters, 384*, 165-177.
756 doi:https://doi.org/10.1016/j.epsl.2013.10.013
757 Worthington, J. R., Hacker, B. R., & Zandt, G. (2013). Distinguishing eclogite from peridotite:
758 EBSD-based calculations of seismic velocities. *Geophysical Journal International,*
759 *193*(1), 489-505. doi:https://doi.org/10.1093/gji/ggt004
760 Yamato, P., Duretz, T., & Angiboust, S. (2019). Brittle/ductile deformation of eclogites: insights
761 from numerical models. *Geochemistry, Geophysics, Geosystems, 20*, 3116– 3133.
762 doi:https://doi.org/10.1029/2019gc008249
763 Yuan, X., Sobolev, S. V., Kind, R., Oncken, O., Bock, G., Asch, G., . . . Comte, D. (2000).
764 Subduction and collision processes in the Central Andes constrained by converted
765 seismic phases. *Nature, 408*, 958–961. doi:https://doi.org/10.1038/35050073
766 Zertani, S., John, T., Tilmann, F., Motra, H. B., Keppler, R., Andersen, T. B., & Labrousse, L.
767 (2019a). Modification of the seismic properties of subducting continental crust by
768 eclogitization and deformation processes. *Journal of Geophysical Research: Solid Earth,*
769 *124*, 9731-9754. doi:https://doi.org/10.1029/2019jb017741
770 Zertani, S., Labrousse, L., John, T., Andersen, T. B., & Tilmann, F. (2019b). The Interplay of
771 Eclogitization and Deformation During Deep Burial of the Lower Continental Crust—A
772 Case Study From the Bergen Arcs (Western Norway). *Tectonics, 38*(3), 898-915.
773 doi:https://doi.org/10.1029/2018tc005297
774 Zhong, X., Andersen, N. H., Dabrowski, M., & Jamtveit, B. (2019). Zircon and quartz inclusions
775 in garnet used for complementary Raman thermobarometry: application to the Holsnøy
776 eclogite, Bergen Arcs, Western Norway. *Contributions to Mineralogy and Petrology,*
777 *174*(6), 50. doi:https://doi.org/10.1007/s00410-019-1584-4

778